Journal of The Electrochemical Society, 2022 **169** 040556
1945-7111/2022/169(4)/040556/10/$40.00 © 2022 The Electrochemical Society ("ECS"). Published on behalf of ECS by IOP Publishing Limited

Effective Representation of Active Material and Carbon Binder in Porous Electrodes

Weiyu Li and Daniel M. Tartakovsky[z]

Department of Energy Resources Engineering, Stanford University, Stanford, California 94305, United States of America

Active cathode material and graphite anode material are routinely mixed with conductor and binder to improve the electric conductivity and mechanical stability of electrodes. Despite its benefits, this carbon binder domain (CBD) impedes ionic transport and reduces the active surface area, thus impacting the battery performance. We consider a composite spherical particle, whose active-material core is coated with CBD, and its homogeneous counterpart, for which we derived equivalent electrical conductivity, ionic diffusivity, and reaction parameters in the Butler-Volmer equation. These equivalent characteristics are defined to ensure that the same mass and charge enter the composite and homogenized spheres. They are expressed in terms of the volume fraction of the active material and transport properties of the active material and CBD. In general, the equivalent effective diffusion coefficient and reaction parameters are time-dependent and exhibit two-stage behavior characterized by the reaction delay time. At later times, these characteristics are time-independent and given explicitly by closed-form formulae. The simplicity of these expressions facilitates their use in single- and multi-particle representations of Li-ion and Li-metal batteries.
 [DOI: 10.1149/1945-7111/ac6832]

Manuscript submitted March 8, 2022; revised manuscript received March 30, 2022. Published April 27, 2022.

Rechargeable Li-ion and Li-metal batteries are among the most effective and promising energy storage devices for portable electronics and electric vehicles. While their anode materials differ (graphite and Li metal in the case of Li-ion and Li-metal batteries, respectively), both battery types use the same lithium intercalation cathode materials,[1] such as lithium cobalt oxide, lithium nickel manganese cobalt oxide, lithium manganese oxide, or lithium iron phosphate. Continued improvement of porous cathodes requires the ability to model both microscopic (pore-scale) electrochemical processes and their impact on battery performance.

Active cathode material particles, as well as graphite anode material particles, are often mixed with conducting material (e.g., carbon black) and binder to improve the electric conductivity and mechanical stability of electrodes.[2–5] During the manufacturing process, conductive additive and binder form the so-called carbon binder domain (CBD), a mixed phase surrounding active particles. Despite its benefits, CBD impedes ionic transport in the electrode by increasing the tortuosity of diffusion pathways and reducing the active surface area, thus impacting the battery performance.[6–8]

Advances in imaging techniques have enabled one to resolve the spatial extent of CBD in a composite electrode.[6,8–11] This, in turn, made it possible to assess the impact of CBD on effective transport properties either via direct tortuosity[7,11] and impedance[12] measurements, or via microstructure-resolving simulations of Li-ion transport and electrochemical transformations.[9] Although such pore-scale models accurately capture the relevant processes in tiny volumes comprising a few CBD-coated active particles and electrolyte, they are too computationally expensive to be used at the device scale. This motivated the development of their macroscopic counterparts such as the single particle models (SPMs),[13–16] the Doyle-Fuller-Newman (DFN) model[17] or homogenized models.[18–20] These and similar macroscopic models seldom account for the presence of CBD. A notable exception is the study[21] that used charge transfer resistance measurements to relate changes in the reaction rate constant to changes in the volume fractions of active material and CBD in the cathode, although ionic transport in CBD was ignored.

Yet, the latter is of paramount importance to battery performance. For example, the overall electrode ionic conductivity is more strongly tied to the volume fraction and ionic conductivity of CBD than to its overall porosity.[6] This suggests the need for a mathematical model that relates measurable characteristics of active particles and CBD, such as their volume fractions and transport properties (diffusion coefficients, ionic conductivities, etc.) to the bulk properties of the composite electrode material (effective diffusion coefficients, ionic conductivities, etc.).

Complex microstructures of composite materials can be represented via an assemblage of coated spheres.[22] This strategy can be used to model the composite electrode as a collection of spherical grains of active material coated by CBD, with resulting pores filled by electrolyte. For linear systems, the Hashin-Shtrikman bounds provide the effective conductivity bounds for an isotropic two-component material composed of coated spheres,[23] while the Wiener arithmetic and harmonic means give the upper and lower bounds for the effective conductivity of anisotropic media with multiple components.[22] These theoretical results have impacted a wide range of linear and nonlinear problems,[24–26] but are of limited use in battery modeling, since they do not guarantee the mass and charge conservation in the presence of ion intercalation into active particles.

Our study fills this void by presenting an equivalent/homogenized model of ion transport and intercalation for a spherical active particle coated by CBD and immersed into electrolyte under galvanostatic condition. The model conserves mass and charge, and results in semi-analytical expressions for equivalent ionic conductivity, diffusion coefficient, and reaction rate of the composite (active material/CBD) particle. These equivalent characteristics are expressed in terms of the volume fractions and transport properties of the constitutive phases; they take a closed form at large times. Our results for a CBD-coated $LiNi_{0.6}Mn_{0.2}Co_{0.2}O_2$ (NMC622) active particle with the volume fraction of 0.8, 0.85, and 0.9 exhibit the relative error in Li ion accumulation of less than 1% for C rates ranging from 0.1 C to 10 C.

Our effective model is important in its own right when used in the single-particle models. It also can serve as input for the DFN model and homogenized macroscopic dual-continua models. Hence, it is of direct relevance to cell-level performance simulation and optimization.

Problem Formulation

Continuum or Darcy-scale treatments of porous media represent irregular grains and complex pore structures as ordered assemblages of regular shaped objects, e.g., periodic arrangements of spheres or ellipses.[20,22,27] That is because any structural irregularity averages out over a representative elementary volume that contains thousands or millions of grains. With that in mind, we consider a spherical active particle of radius r_1 that is coated with the CBD layer, giving rise to the composite sphere of radius r_2 (Fig. 1). The active material has diffusion coefficient D_1 ($m^2\ s^{-1}$) and ionic conductivity K_1

[z]E-mail: tartakovsky@stanford.edu

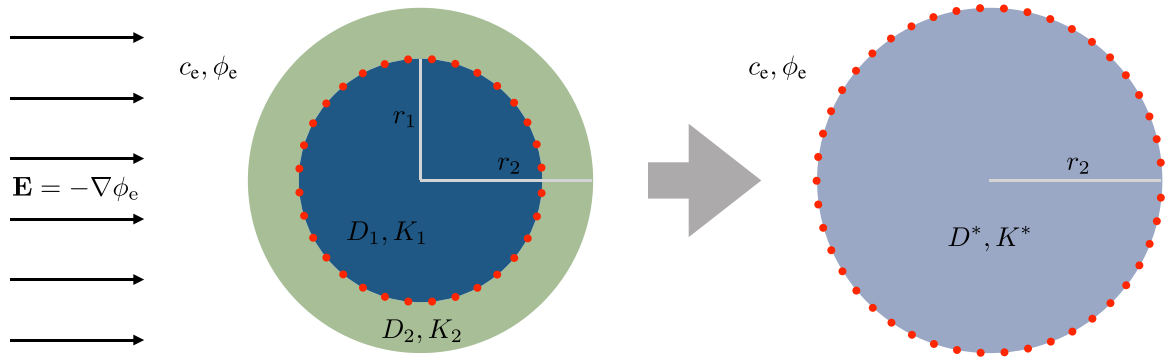

Figure 1. Left: Spherical composite particle of radius r_2 comprising an active material core of radius r_1 coated with a CBD layer. The active material has diffusion coefficient D_1 and ionic conductivity K_1; the corresponding quantities for CBD are denoted by D_2 and K_2. **Right:** Its homogeneous counterpart with equivalent diffusion coefficient D^* and ionic conductivity K^*. The red lines denote locations of the intercalation surface. The sphere is immersed in the electrolyte with Li-ion concentration c_e, electric potential ϕ_e, and uniform electric field $\mathbf{E} = -\nabla\phi_e$.

(S m^{-1}); the corresponding quantities for CBD are denoted by D_2 and K_2. Li-ion intercalation takes place at the active particle's surface, i.e., at $r = r_1$. The sphere is immersed into the electrolyte with Li-ion concentration c_e and electric potential ϕ_e; a uniform electric field $\mathbf{E}$ in the x direction represents the electric field in a working battery's electrode. Indeed, visualization of the electric potential distribution across working devices shows the electric potential profile in the porous electrode has an approximately linear slope, which corresponds to a uniform electric field, $\mathbf{E} = -\nabla\ \phi_e$.[28] The single particle model[13] predicts a similar linear electric potential distribution in the electrode.

An equivalent representation of this composite particle is a homogeneous sphere of radius r_2 that has diffusion coefficient D^*, ionic conductivity K^*, and ion intercalation at its surface. These characteristics are such that the two spheres have the same current density and ion flux through their respective surfaces. Our goal is to express these equivalent parameters in terms of the volume fractions ($V_1 = r_1^3/r_2^3$ and $V_2 = 1 - V_1$) and transport properties of each phase.

Transport in active core and CBD coating.—Given the geometry of the composite particles, we use the spherical coordinate system $\mathbf{r} = (r, \theta, \varphi)^\intercal$. Spatiotemporal evolution of the molar concentrations of Li ions (mol m^{-3}) in the active material, $c_1(\mathbf{r}, t)$ with $0 \leqslant r \leqslant r_1$, and the CBD coating, $c_2(\mathbf{r}, t)$ with $r_1 \leqslant r \leqslant r_2$, is described by the diffusion equations[12]

$$\frac{\partial c_i}{\partial t} = -\nabla\cdot\mathbf{J}_{\mathrm{dif},i},\ \ \mathbf{J}_{\mathrm{dif},i} = -D_i\nabla c_i,\quad i = 1, 2. \tag{1}$$

The corresponding electrical potentials (V) in each phase, $\phi_1(\mathbf{r}, t)$ with $0 \leqslant r \leqslant r_1$ and $\phi_2(\mathbf{r}, t)$ with $r_1 \leqslant r \leqslant r_2$, are governed by the Laplace equations

$$\nabla\cdot\mathbf{J}_{\mathrm{el},i} = 0,\ \ \mathbf{J}_{\mathrm{el},i} = -K_i\nabla\phi_i,\quad i = 1, 2. \tag{2}$$

These two sets of equations are defined on $0 < r < r_1$ for $i = 1$, and on $r_1 < r < r_2$ for $i = 2$; both for time $t > 0$. They are coupled by enforcing the continuity of the radial components of the mass fluxes, $\mathbf{J}_{\mathrm{dif},i}$, and current densities, $\mathbf{J}_{\mathrm{el},i}$, at the interface $r = r_1$:[29]

$$D_1\frac{\partial c_1}{\partial r} = D_2\frac{\partial c_2}{\partial r} = R_{\mathrm{int}} \tag{3}$$

and

$$K_1\frac{\partial\phi_1}{\partial r} = K_2\frac{\partial\phi_2}{\partial r} = FR_{\mathrm{int}}. \tag{4}$$

The Butler-Volmer equation with the charge transfer coefficient of 0.5 describes the ion intercalation on the active particle surface,

$$R_{\mathrm{int}} = 2k_1\sqrt{c_1c_2\left(1 - \frac{c_1}{c_{1,\max}}\right)}\ \sinh\left[\frac{F}{2RT}(\phi_1 - \phi_2 - U(c_1/c_{1,\max}))\right], \tag{5}$$

where k_1 is the reaction rate constant of the active material (m/s), $c_{1,\max}$ is the maximum Li concentration that could be stored in the active particle (mol m^{-3}), U is the open circuit potential (V) that depends on the Li filling fraction $c_1/c_{1,\max}$, F is the Faraday constant (s·A/mol), R is the gas constant (J/mol/K), and T is the temperature (K).

At the interface between the composite particle and liquid electrolyte, $r = r_2$, we assume charge neutrality and the electrolyte to be dilute.[29] This gives rise to the boundary conditions at $r = r_2$,

$$D_e\frac{\partial c_e}{\partial r} + \frac{t_+^2K_e}{F^2}\frac{\partial\mu_e}{\partial r} + \frac{K_et_+}{F}\frac{\partial\phi_e}{\partial r} = D_2\frac{\partial c_2}{\partial r}, \tag{6}$$

$$\frac{t_+K_e}{F}\frac{\partial\mu_e}{\partial r} + K_e\frac{\partial\phi_e}{\partial r} = K_2\frac{\partial\phi_2}{\partial r}, \tag{7}$$

and

$$c_e = c_2,\qquad \phi_e = \phi_2, \tag{8}$$

where $c_e(\mathbf{r})$ and $\phi_e(\mathbf{r})$ are respectively the Li ion concentration (mol m^{-3}) and electrical potential (V) in the electrolyte, $r \geqslant r_2$; and D_e, K_e, and t_+ denote the interdiffusion coefficient (m^2 s^{-1}), the ionic conductivity (S m^{-1}), and the transfer coefficient (−) of Li ions in the electrolyte, respectively. $\mu_e = RT\ln(fc_e)$, is the chemical potential of Li ions in the electrolyte, where f is the activity coefficient. The interfacial electric potential in the electrolyte (at $r = r_2$) varies with the angle θ, in response to the uniform electrical current imposed in the x_1 direction far away from the sphere (Fig. 1).

The problem formulation is completed by specifying the boundary and initial conditions

$$c_1(r = 0, t) < \infty;\quad \phi_1(r = 0, t) < \infty\ ;\qquad c_i(\mathbf{r}, 0) = c_{\mathrm{in}},\quad i = 1, 2. \tag{9}$$

Transport in equivalent particle.—The equivalent model treats the composite particle as a homogeneous material with equivalent diffusion coefficient D^* and equivalent ionic conductivity K^* (Fig. 1). Equations 1 and 2 are replaced with

$$\frac{\partial c}{\partial t} = D^*\nabla^2 c,\ K^*\nabla^2\phi = 0, \quad [10]$$

and describe the spatiotemporal evolution of Li concentration, $c(r, t)$, and electric potential, $\phi(r, t)$, in the whole particle, i.e., for $0 < r < r_2$. To ensure that the same Li ion flux and the same current density enter the composite particle and its equivalent counterpart, we replace the interfacial and boundary conditions 3–7 with the boundary conditions at $r = r_2$,

$$D_e\frac{\partial c_e}{\partial r} + \frac{t_+^2 K_e}{F^2}\frac{\partial \mu_e}{\partial r} + \frac{K_e t_+}{F}\frac{\partial \phi_e}{\partial r} = D^*\frac{\partial c}{\partial r} = R_{int}^*, \quad [11]$$

$$\frac{t_+ K_e}{F}\frac{\partial \mu_e}{\partial r} + K_e\frac{\partial \phi_e}{\partial r} = K^*\frac{\partial \phi}{\partial r} = FR_{int}^*, \quad [12]$$

where

$$R_{int}^* = 2k^*\sqrt{cc_e\left(1 - \frac{c}{c_{max}}\right)} \sinh\left[\frac{F}{2RT}(\phi - \phi_e - U(c/c_{max}))\right], \quad [13]$$

k^* is the equivalent reaction rate constant, and c_{max} is the maximum Li concentration that can be stored in the homogenized particle. In analogy with 9, we also require

$$c(r = 0, t) < \infty; \quad \phi(r = 0, t) < \infty\ ; \quad c(\mathbf{r}, 0) = c_{in}. \quad [14]$$

The interfacial conditions 6–8 and 11–13 should hold for all interfacial values of (gradients of) ion concentration, $c_e(r_2, \cdot\ )$, and electric potential, $\phi_e(r_2, \cdot\ )$, in the liquid electrolyte. Consequently, for the purpose of homogenization, we treat them as given rather than computed as solutions of the Nernst-Planck equations. That is in contrast to fully-resolved pore-scale simulations that comprise a couple system of equations for the active particle, CBD, and the electrolyte-filled pore space.

Equivalent Models of Solid Phase

The equivalent representation of the composite particle in Fig. 1 shifts the intercalation surface from $r = r_1$ to $r = r_2$. To ensure that this procedure results in global conservation of mass and charge, we introduce the following relations on the respective intercalation surfaces:

$$r_1^2 D_1\frac{\partial c_1}{\partial r}(r_1, t) = r_2^2 D^*\mathcal{H}(t - \tau)\frac{\partial c}{\partial r}(r_2, t - \tau) \quad [15]$$

$$r_1^2 K_1\frac{\partial \phi_1}{\partial r}(r_1, t) = r_2^2 K^*\mathcal{H}(t - \tau)\frac{\partial \phi}{\partial r}(r_2, t - \tau), \quad [16]$$

where $\mathcal{H}(\cdot)$ is the Heaviside function. The reaction delay time $\tau = (r_2 - r_1)^2/D_2$ accounts for the shift of the reaction interface from the inner radius $r = r_1$ to the outer radius $r = r_2$. Due to the boundary conditions 3, 4, 11, 12 and the Butler-Volmer relations 5 and 13, the two interfacial conditions 15 and 16 collapse into one:

$$r_1^2 R_{int}(r_1, t) = r_2^2\mathcal{H}(t - \tau)R_{int}^*(r_2, t - \tau). \quad [17]$$

This definition of the equivalent Butler-Volmer rate is automatically satisfied by imposing the following relations on the respective intercalation surfaces:

$$\phi_1(r_1, t) - \phi_2(r_1, t) = \phi(r_2, t) - \phi_e(r_2, t), \quad [18a]$$

$$\frac{c_1(r_1, t)}{c_{1,max}} = \mathcal{H}(t - \tau)\frac{c(r_2, t - \tau)}{c_{max}^*}, \quad [18b]$$

$$r_1^2 k_1\sqrt{c_{1,max}c_2(r_1, t)} = r_2^2 k^*\mathcal{H}(t - \tau)\sqrt{c_{max}^* c_e(r_2, t - \tau)}. \quad [18c]$$

These relations define the equivalent parameters c_{max} and k^*.

Equivalent ionic conductivity.—Our derivation of the equivalent ionic conductivity K^* follows that of the coated sphere model.[22] The key difference between our problem and the model[22] is that the interface between the two materials is now reactive. Consequently, we replace the continuity of electric potential at $r = r_1$ with the potential-drop condition 18a and enforce the charge conservation condition 16.

Assuming the azimuthal symmetry, we rewrite the Laplace Eqs. 2 and 10 in polar coordinates $\mathbf{r} = (r, \theta)^\top$ and look for their solutions, $\phi_i(\mathbf{r})$ with $i = 1, 2$ and $\phi^*(\mathbf{r})$, in the form $\phi_1 = a_1 r\cos\theta$ for $0 \leqslant r \leqslant r_1$; $\phi_2 = (a_2 r + b_2/r^2)\cos\theta$ for $r_1 \leqslant r \leqslant r_2$; and $\phi^* = a\ r\cos\theta$ for $0 < r < r_2$; where a_1, a_2, b_2, and a are the constants of integration. These are obtained from the conditions of continuity of the radial components of the current densities $\mathbf{J}_{el,1}$ and $\mathbf{J}_{el,2}$ at $r = r_1$ in Eq. 4,

$$K_1 a_1 = K_2(a_2 - 2b_2/r_1^3); \quad [19]$$

and of the radial components of the current densities $\mathbf{J}_{el,2}$ and $\mathbf{J}_{el}^*$ at $r = r_2$ in Eqs. 7 and 12,

$$K^* a = K_2(a_2 - 2b_2/r_2^3). \quad [20]$$

The remaining two equations arise from the conservation of charge, Eq. 16,

$$r_2^2 K^* a = r_1^2 K_1 a_1; \quad [21]$$

and the drop of the electrical potential across the reaction interfaces, Eqs. 18a and 8,

$$a_1 r_1 - (a_2 r_1 + b_2/r_1^2) = a\ r_2 - (a_2 r_2 + b_2/r_2^2). \quad [22]$$

The system of linear algebraic Eqs. 19–22 has a nontrivial solution if and only if

$$K^* = \frac{2K_1K_2}{K_1\frac{r_2/r_1 - 1}{1 - r_1r_2/(r_1 + r_2)^2} + 2K_2r_2\Big/r_1} = \frac{2K_1K_2}{K_1\frac{V_1^{-1/3} - 1}{1 - V_1^{1/3}/(V_1^{1/3} + 1)^2} + 2K_2/V_1^{1/3}}. \quad [23]$$

If the sphere consists entirely of the active material, i.e., if $V_1 = 1$, then this expression reduces to $K^* = K_1$, as it should.

Equivalent diffusion coefficient.—The subsequent analysis is facilitated by considering galvanostatic conditions, under which a constant current I_a (corresponding to the current density $J = I_a/(4\pi r_2^2)$ is applied at the sphere's surface, $r = r_2$. Then, the boundary conditions 6 and 11 are replaced with

$$D_2\frac{\partial c_2}{\partial r}(r_2, t) = \frac{I_a}{4\pi r_2^2 F} \text{ and } D^*\frac{\partial c}{\partial r}(r_2, t) = \frac{I_a}{4\pi r_2^2 F}, \quad [24]$$

and the solutions to the corresponding boundary value problems are independent from the azimuth and polar angles, $c_i = c_i(r, t)$ with

$i = 1, 2$, and $c = c(r, t)$. Without loss of generality, we set the initial concentration to $c_{in} = 0$ (otherwise, one can repeat our analysis for $c_i - c_{in}$ and $c - c_{in}$). Then, the Laplace-transformed solutions of the diffusion Eq. 1, written in the spherical coordinates and subject to the auxiliary conditions 3, 9, 15 and 24 are (see Appendix for detail)

$$\hat{c}_1(r, \lambda) = \frac{Jr_2^2}{FD_1 r\lambda}\alpha_1(e^{r\sqrt{\lambda/D_1}} - e^{-r\sqrt{\lambda/D_1}}), \quad 0 \leqslant r \leqslant r_1, \tag{25a}$$

$$\hat{c}_2(r, \lambda) = \frac{Jr_2^2}{FD_2 r\lambda}[\alpha_2 e^{-(r_2-r)\sqrt{s}} + \beta_2 e^{-(r-r_1)\sqrt{s}}], \quad r_1 \leqslant r \leqslant r_2, \tag{25b}$$

where λ is the Laplace-transform variable, $s = \lambda D_2$, $\beta = r_2 - r_1$, and

$$\alpha_1 = \frac{e^{-\lambda\tau}}{(r_1\sqrt{\lambda/D_1} + 1)e^{-r_1\sqrt{\lambda/D_1}} + (r_1\sqrt{\lambda/D_1} - 1)e^{r_1\sqrt{\lambda/D_1}}}, \tag{25c}$$

$$\alpha_2 = \frac{r_1 + 1/\sqrt{s} - e^{-D_2\tau s - \beta\sqrt{s}}(r_2 + 1/\sqrt{s})}{(r_2 - 1/\sqrt{s})(r_1\sqrt{s} + 1) - (r_1 - 1/\sqrt{s})e^{-2\beta\sqrt{s}}(r_2\sqrt{s} + 1)}, \tag{25d}$$

$$\beta_2 = \frac{e^{-\beta\sqrt{s}}(r_1 - 1/\sqrt{s}) - e^{-D_2\tau s}(r_2 - 1/\sqrt{s})}{(r_2 - 1/\sqrt{s})(r_1\sqrt{s} + 1) - (r_1 - 1/\sqrt{s})e^{-2\beta\sqrt{s}}(r_2\sqrt{s} + 1)}. \tag{25e}$$

We compute the inverse Laplace transforms, $c_1(r_1, t)$ and $c_2(r_2, t)$, either numerically via the subroutine `INVLAP`[30] from the MATLAB File Exchange or analytically for large times t and steady state, as described below.

Diffusivity of an equivalent medium is known to be time-dependent, at least at early times.[31] We account for this possibility by treating $D^* = D^*(t)$. We show in the Appendix that the Laplace-transformed Li-ion concentration $\hat{c}(r, \lambda_T)$ is given by

$$\hat{c}(r, \lambda_T) = \frac{Jr_2^2}{Fr}\frac{\sinh(r\sqrt{\lambda_T})}{r_2\sqrt{\lambda_T}\cosh(r_2\sqrt{\lambda_T}) - \sinh(r_2\sqrt{\lambda_T})}\int_0^\infty \frac{e^{-\lambda_T T}}{D^*(h(T))}\,dT, \tag{26}$$

where λ_T is the Laplace-transform variable, and $t = h(T)$ is given implicitly by $T = \int_0^t D^*(t')dt'$. The inverse Laplace transform, $\mathcal{L}_T^{-1}$, of $\hat{c}(r, \lambda_T)$ in Eq. 27 is given by the convolution,

$$c(r, T) = \frac{Jr_2^2}{Fr}\int_0^T \frac{w(r, T-\nu)}{D^*(h(\nu))}d\nu, \tag{27a}$$

where

$$w(r, T) = \mathcal{L}_T^{-1}\left\{\frac{\sinh(r\sqrt{\lambda_T})}{r_2\sqrt{\lambda_T}\cosh(r_2\sqrt{\lambda_T}) - \sinh(r_2\sqrt{\lambda_T})}\right\}. \tag{27b}$$

We define $D^*(t)$ as the diffusion coefficient of the homogenized sphere that, under galvanostatic conditions 24, results in the surface Li-ion concentration $c(r_2, T)$ that equals the weighted average of the Li-ion concentrations on the surfaces $r = r_1$ and $r = r_2$ of the composite sphere, i.e.,

$$c(r_2, t) = V_1 c_1(r_1, t) + (1 - V_1)c_2(r_2, t). \tag{28}$$

This yields a nonlinear integral equation for $D^*(t)$,

$$\frac{Jr_2}{F}\int_0^T \frac{w(r_2, T-\nu)}{D^*(h(\nu))}d\nu = V_1 c_1(r_1, t) + (1 - V_1)c_2(r_2, t), \quad T = \int_0^t D^*(t')dt', \tag{29}$$

which is solved numerically using Algorithm 1 in the Appendix.

Equivalent rate and maximum concentration.—Combining Eqs. 18b and 18c with Eq. 28 we obtain expressions for the remaining homogenized parameters, $c^*_{max}(t)$ and $k^*(t)$,

$$\frac{c^*_{max}(t)}{c_{1,max}} = \frac{V_1 c_1(r_1, t) + (1 - V_1)c_2(r_2, t)}{c_1(r_1, t + \tau)}, \quad \frac{k^*(t)}{k_1} = \frac{r_1^2}{r_2^2}\sqrt{\frac{c_{1,max}c_2(r_1, t + \tau)}{c^*_{max}(t)c_2(r_2, t)}}. \tag{30}$$

Closed-form asymptotic expressions.—For large t, the time-dependent equivalent diffusion coefficient D^* reaches its constant value. We show in the Appendix that it is given by the weighted harmonic mean of D_1 and D_2,

$$D^* = \left\{\frac{V_1^{2/3}}{D_1} + 5\frac{1 - V_1}{D_2}\left[\frac{(1 - V_1^{1/3})^2 + 3(V_1^{1/3} + 2)(1 - V_1^{1/3})}{2(1 - V_1^{1/3})^2 + 6V_1^{1/3}} - \frac{3(1 - V_1^{1/3})^2}{1 - V_1}\right]\right\}^{-1}. \tag{31}$$

We also show that

$$\frac{c^*_{max}(t)}{c_{1,max}} \approx V_1 \tag{32}$$

and

$$\frac{k^*(t)}{k_1} \approx V_1^{7/6}\sqrt{\frac{1 + 2V_1^{1/3}}{7 + 2V_1^{1/3}}}. \tag{33}$$

Results and Discussion

Figure 2 exhibits the equivalent ionic conductivity K^*, given by Eq. 23, for different values of K_1 and K_2 and several volume fractions V_1 of the active material. As V_1 decreases, the composite material contains more CBD and K^* becomes progressively smaller than the ionic conductivity of the active material, K_1. For example, if CBD has ionic conductivity $K_2 = 1$ S m^{-1} and its volume fraction in the mixture is $V_2 = 0.3$, then the equivalent ionic K^* is about half of the ionic conductivity of the active material, $K_1 = 10$ S m^{-1}.

We use Algorithm 1 to solve Eq. 29, i.e., to compute the dimensionless equivalent diffusivity $\tilde{D}^*(\tilde{t}) = D^*/D_1$ as function of the dimensionless time $\tilde{t} = tD_1/r_2^2$. In this calculation, we use the time step $\Delta\tilde{t} = 10^{-3}$, $\tilde{t}_k = k\Delta\tilde{t}$, and MATLAB's subroutine `fsolve` with termination tolerance 10^{-6} to find the root of Eq. 29; the Li-ion concentrations are normalized with the maximum Li concentration in active particle $c_{1,max}$ such that $\tilde{c} = c/c_{1,max}$ and $\tilde{c}_i = c_i/c_{1,max}$ with $i = 1, 2$; and the dimensionless current density $\tilde{J} = Jr_2/(FD_1c_{1,max})$ serves as the sole input. A value of the applied current density $\tilde{J}$ does

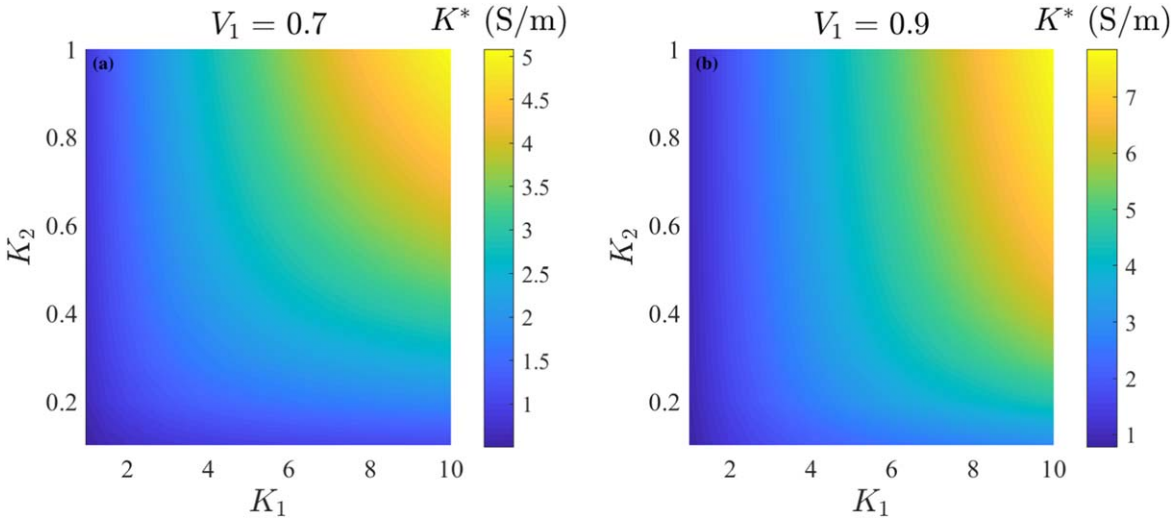

Figure 2. Equivalent ionic conductivity of the composite material composed of the active material and CBD with ionic conductivities K_1 and K_2, respectively. The active material's volume fraction in the mixture, V_1, is **(a)** 0.7 and **(b)** 0.9.

not affect the magnitude of the equivalent parameters, it only alters the values of the concentrations $\tilde{c}_i$ and $\tilde{c}$ and, thus, the time it takes the sphere to reach its maximum Li-storing capacity. To be specific, we set $\tilde{J} = 1$ in the simulation results presented below.

The results of this calculation, $\tilde{D}^* = \tilde{D}^*(\tilde{t})$, are shown in Fig. 3 for several combinations of the active material's volume fraction V_1 and the diffusion coefficient ratios D_2/D_1. (Unless specified otherwise, we use $D_2/D_1 = 0.0178$ as a reference value[12].) The equivalent diffusivity $\tilde{D}^*(\tilde{t})$ increases at times preceding the intercalation delay time $\tilde{\tau} = (r_2 - r_1)^2 D_1/(D_2 r_2^2)$; drops appreciably at $\tilde{t} = \tilde{\tau}$; and then increases a bit to reach its steady-state value. The time to steady state decreases with V_1 (Fig. 3a); for $V_1 = 0.99$, CBD's volume fraction is so small that $\tilde{D}^* \approx 1$, as expected. The chemical composition of CBD, as encapsulated in the value of the diffusion coefficient D_2, affects the transitional behavior and the steady state value of D^* (Fig. 3b).

We found a close agreement between the steady-state values of the equivalent diffusion coefficient $\tilde{D}^*$ computed numerically with Eq. 29 and analytically via the closed-form expression 31 (see Fig. 7 in the Appendix). For the latter to be useful in battery-scale models, it must provide an accurate approximation of the Li-ion flux through the composite sphere's surface, $J_{\text{dif}}(r_2, t) = -D_2 \partial_r c_2(r_2, t)$, i.e., it must conserve mass. Note that the effective model with time-dependent $D^*(t)$ in Eq. 29 is mass-conservative by construction, so that the replacement of $D^*(t)$ with its steady-state counterpart D^* in Eq. 31 is the only source of error. Let $J^*_{\text{dif}}(r_2, t) = -D^* \partial_r c(r_2, t)$ denote the Li-ion flux through the surface of a homogeneous sphere whose diffusion coefficient D^* is given by Eq. 31. The ratio $J^*_{\text{dif}}/J_{\text{dif}}$ is shown in Fig. 4a as function of dimensionless time $\tilde{t}$, for several values of V_1. The discrepancy between J^*_{dif} and J_{dif} is confined to early times $\tilde{t}$; it becomes smaller but more persistent as the active material's volume fraction decreases.

Another measure of discrepancy is the relative error in Li-ion accumulation,

$$\mathcal{E}_{\text{tot}} = \left| \frac{\int_0^{t_{\max}} J_{\text{dif}}\, \mathrm{dt} - \int_0^{t_{\max}} J^*_{\text{dif}}\, \mathrm{dt}}{\int_0^{t_{\max}} J_{\text{dif}}\, \mathrm{dt}} \right|,$$

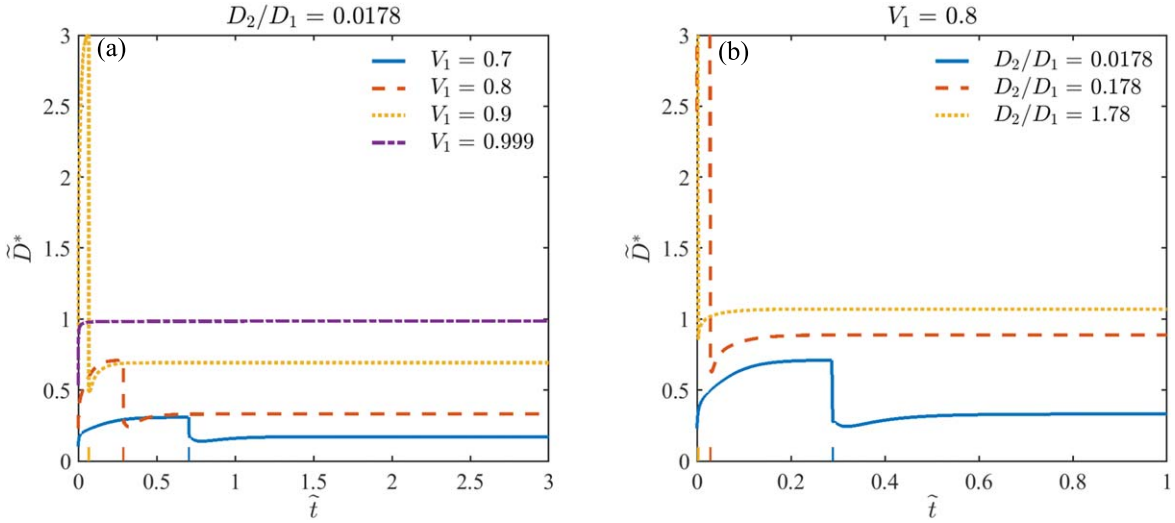

Figure 3. Temporal evolution of the normalized equivalent diffusivity $\tilde{D}^*(\tilde{t})$ for **(a)** several volume fractions of the active material, V_1, and $D_2/D_1 = 0.0178$; and **(b)** several diffusion coefficient ratios D_2/D_1 and $V_1 = 0.8$. The elevated tick marks indicate the dimensionless intercalation delay time $\tilde{\tau} = (r_2 - r_1)^2 D_1/(D_2 r_2^2) = 0.706$, 0.289 and 0.067 for $V_1 = 0.7$, 0.8 and 0.9, respectively.

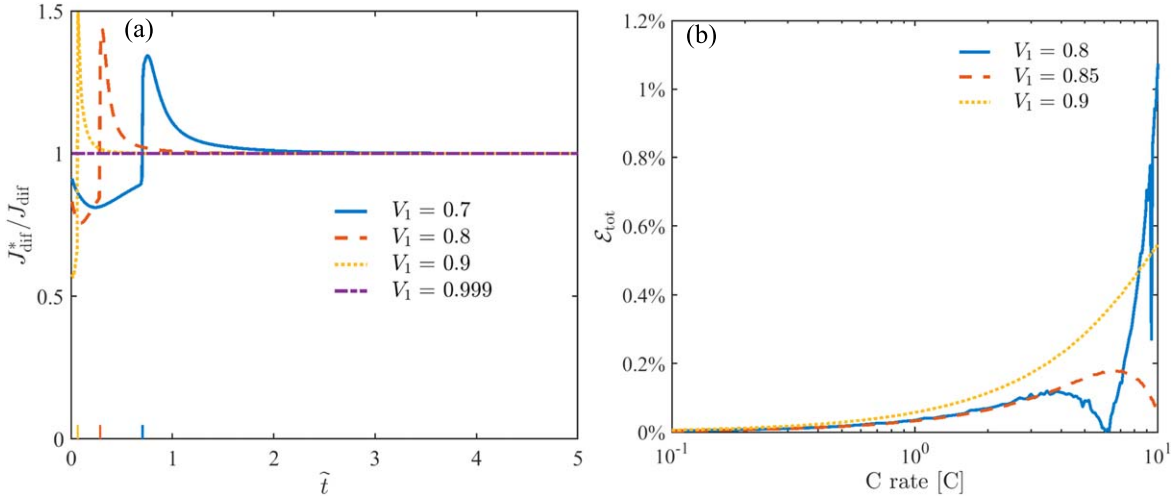

Figure 4. **(a)** Temporal evolution of the ratio between the Li-ion fluxes through the surface, $r = r_2$, of the composite sphere and its homogenized counterpart with D^* in Eq. 31, $J^*_{\rm dif}/J_{\rm dif}$, for several volume fractions V_1 and $D_2/D_1 = 0.0178$. The elevated tick marks indicate the dimensionless intercalation delay time $\tilde{\tau} = (r_2 - r_1)^2 D_1/(D_2 r_2^2) = 0.706$, 0.289 and 0.067 for $V_1 = 0.7$, 0.8 and 0.9, respectively. **(b)** The relative error in the prediction of Li-ion accumulation, $\mathcal{E}_{\rm tot}$, obtained via our homogenized solution. The error is plotted as function of C rate, for the active material $LiNi_{0.6}Mn_{0.2}Co_{0.2}O_2$ (NMC622) with parameters[32] $D_1 = 4.3032 \cdot 10^{-14}$ m^2 s^{-1}, $c_{1,\max} = 50451$ mol m^{-3}, $D_2 = 7.66 \cdot 10^{-16}$ m^2 s^{-1} and $r_2 = 5$ μm; and several values of the volume fraction V_1.

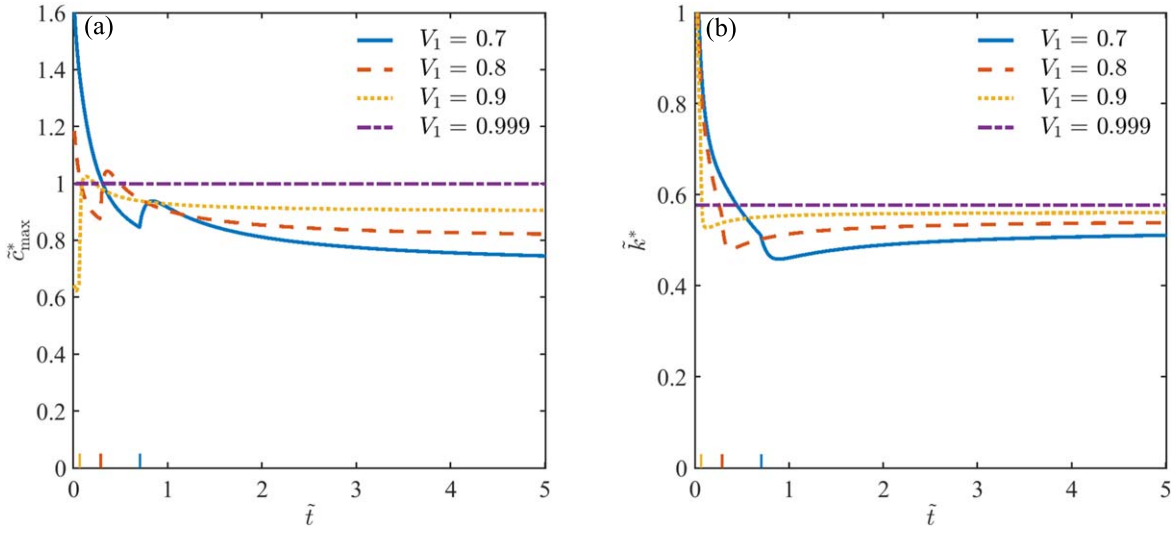

Figure 5. Temporal evolution of **(a)** maximum Li concentration $\tilde{c}^*_{\max}(\tilde{t}) = c^*_{\max}(\tilde{t})/c_{1,\max}$ and **(b)** reaction rate constant $\tilde{k}^*(\tilde{t}) = k^*(\tilde{t})/k_1$, for several volume fractions of the active material, V_1. The ratio between the diffusion coefficients of the inactive and inactive materials is set to[12] $D_2/D_1 = 0.0178$. The elevated tick marks indicate the dimensionless intercalation delay time $\tilde{\tau} = (r_2 - r_1)^2 D_1/(D_2 r_2^2) = 0.706$, 0.289 and 0.067 for $V_1 = 0.7$, 0.8 and 0.9, respectively.

where $t_{\max}$ is the total discharge (charge) time, i.e., the time to achieve the maximum Li-ion concentrations $c_{1,\max}$ and $c^*_{\max}$ in both the active particle and its equivalent counterpart. Figure 4b displays $\mathcal{E}_{\rm tot}$ as function of C rate, for the active material $LiNi_{0.6}Mn_{0.2}Co_{0.2}O_2$ (NMC622) whose properties are[32] $D_1 = 4.3032 \cdot 10^{-14}$ m^2 s^{-1}, $c_{1,\max} = 50451$ mol m^{-3}, $D_2 = 7.66 \cdot 10^{-16}$ m^2 s^{-1} and $r_2 = 5$ μm. For these parameter values and for $V_1 = 0.8$, 0.85 and 0.9, 1C rate corresponds to the current density $J = 1.8728$ A m^{-2}, 1.9458 A m^{-2} and 2.0298 A m^{-2}, respectively. (These values of J are obtained from Eq. 49 with $t = 1$ h and $c_1 = c_{1,\max}$.) The corresponding delay times are $\tau = 0.0466 t_{\max}$, $0.0252 t_{\max}$, and $0.0108 t_{\max}$; in words, the delay time τ is orders of magnitude smaller than the charging/discharging time $t_{\max}$. This result demonstrates the adequacy of our asymptotic (for large t) expression in Eqs. 31–33, since the early time transient stage is negligible in the total charging/discharging process. For C rates varying from 0.1 C to 10 C, the relative error in Li ion accumulation is below 1%, which shows that the constant value of D^* in Eq. 31 is valid for a wide range of C rates.

The remaining equivalent parameters, $\tilde{k}^*(\tilde{t}) = k^*(\tilde{t})/k_1$ and $\tilde{c}^*_{\max}(\tilde{t}) = c^*_{\max}(\tilde{t})/c_{1,\max}$, computed numerically with Eq. 30 are displayed in Fig. 5 for several volume fractions V_1. At early times, $\tilde{t} < \tilde{\tau}$, Li ions diffuse from the electrolyte into the inactive material, causing their concentration $\tilde{c}_2(r, \tilde{t})$ to increase at both $r = r_1$ and $r = r_2$, while the Li concentration in the active particle remains unchanged, $\tilde{c}_1(r, \tilde{t}) = 0$. Starting at the delay time $\tilde{t} = \tilde{\tau}$, Li ions intercalate into the active material, increasing $\tilde{c}_1(r_1, \tilde{t})$ linearly with time, while $\tilde{c}_2(r_1, \tilde{t})$ decreases and $\tilde{c}_2(r_2, \tilde{t})$ increases slowly until reaching their steady-state values. This two-stage behavior translates into the concomitant behavior of $\tilde{k}^*(\tilde{t})$ and $\tilde{c}^*_{\max}(\tilde{t})$ (Fig. 5). The time it takes these two parameters to reach their asymptotes decreases with V_1. For $V_1 = 0.99$, the volume fraction of the CBD phase is so small that $c^*_{\max} \approx c_{1,\max}$, as expected; at the same time, $k^* \neq k_1$ because the intercalation surface $r = r_1$, which separates the active material and CBD in the composite sphere, is shifted to $r = r_2$ and becomes an interface between the equivalent homogeneous particle and the electrolyte.

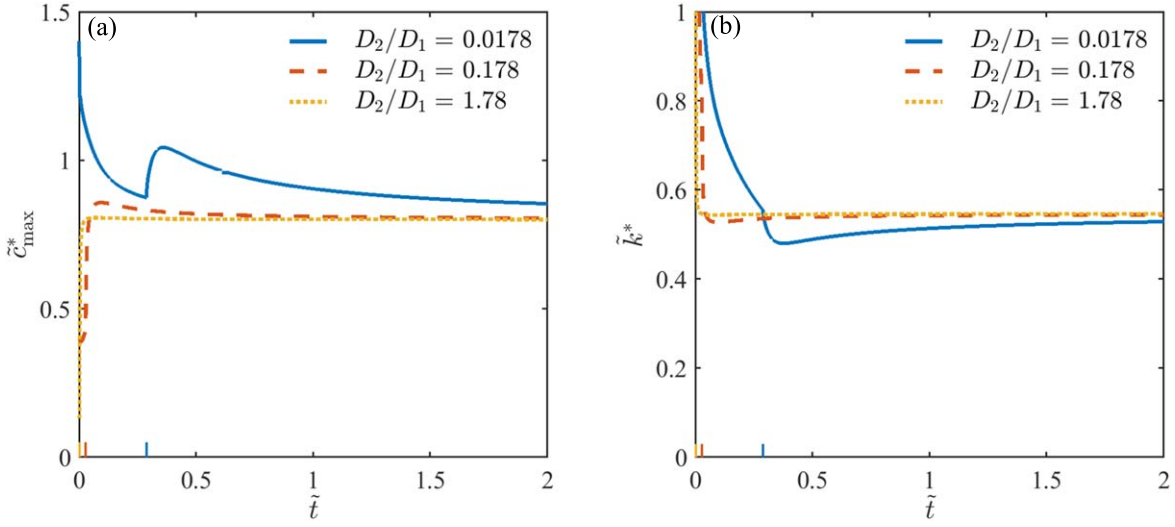

Figure 6. Temporal evolution of **(a)** maximum Li concentration $\tilde{c}^*_{\max}(\tilde{t}) = c^*_{\max}(\tilde{t})/c_{1,\max}$ and **(b)** reaction rate constant $\tilde{k}^*(\tilde{t}) = k^*(\tilde{t})/k_1$, for several values of D_2/D_1. Volume fraction of the active material is set to $V_1 = 0.8$. The elevated tick marks indicate the dimensionless intercalation delay time $\tilde{\tau} = (r_2 - r_1)^2 D_1/(D_2 r_2^2) = 0.289$, 0.029 and 0.003 for $D_2/D_1 = 0.0178$, 0.178 and 1.78, respectively.

The choice of a CBD material, as quantified by the value of its diffusion coefficient D_2, affects the intercalation delay time $\tilde{\tau}$, e.g., for $V_1 = 0.8$, $\tilde{\tau} = 0.289$, 0.029 and 0.003 if $D_2/D_1 = 0.0178$, 0.178 and 1.78, respectively. Thus, the time it takes both $c^*_{\max}(t)$ and $k^*(t)$ to reach their steady state decreases with D_2 (Fig. 6). At the same time, the steady-state values of these equivalent parameters are independent of D_2. Instead, in accordance with Eqs. 32 and 33, the steady-state limit of $c^*_{\max}$ varies linearly with V_1 and that of k^* as the power of V_1.

Conclusions

Our study provides a quantitative assessment of the impact of CBD on overall ionic transport in a composite electrode. The latter was represented by a spherical particle whose active-material core is coated with CBD. This composite sphere is replaced with its homogeneous counterpart, for which we derived equivalent electrical conductivity, ionic diffusivity, and reaction parameters in the Butler-Volmer equation. These equivalent characteristics are defined to ensure that the same mass and charge enter the composite and homogenized spheres. They are expressed in terms of the volume fraction of the active material and transport properties of the active material and CBD. In general, the equivalent effective diffusion coefficient and reaction parameters are time-dependent and exhibit the two-stage behavior characterized by the reaction delay time; their determination requires numerical evaluation of the inverse Laplace transforms. At later times, these characteristics are time-independent and given explicitly by closed-form formulae. Our analysis leads to the following major conclusions.

- Our model can be used to quantitatively assess the effects of CBD on ion transport. For example, for a composite electrode with CBD's volume fraction of 0.2 and the ratio between the diffusion coefficients of CBD and the active material of 0.0178, ignoring the presence of CBD would overestimate the composite's diffusion coefficient by 163%.
- Our closed-form expressions for the equivalent diffusion coefficient and reaction parameters yield accurate approximations of the key quantities of interest. For example, when used to model an NMC622 active particle coated with CBD, they yield predictions of the Li-ion accumulation whose relative error is about 1%, for C rates ranging from 0.1 C to 10 C.
- The simplicity of these expressions facilitates their use in single- and multi-particle representations of Li-ion and Li-metal batteries. This enables one to use these cell-level models, while accounting for the presence of CBD and the physicochemical characteristics of composite electrodes. That, in turn, facilitates the electrode design without resolving the complicated microstructure at high computational cost.

In follow-up studies, we will conduct experimental validation of our model for various active materials, incorporate it into cell-level simulations, and assess its accuracy in predicting cell voltage during discharge. Future extensions of our model will incorporate the volume expansion of active particles and the transport properties of gradient Li-rich oxide cathodes mixed with CBD.

Acknowledgments

This work was supported in part by Hyundai Motor Group and by Air Force Office of Scientific Research under award number FA9550-21-1-0381.

Appendix. Effective Diffusivity

Solution for composite sphere.—Given the azimuth and polar symmetry, Eq. 1 take the form

$$\frac{\partial c_i}{\partial t} = \frac{D_i}{r^2}\frac{\partial}{\partial r}\left(r^2\frac{\partial c_i}{\partial r}\right), \quad i = 1, 2. \qquad [34]$$

The transformation $u_i(r, t) = r c_i(r, t)$ turns Eq. 34 into

$$\frac{\partial u_i}{\partial t} = D_i\frac{\partial^2 u_i}{\partial r^2}, \qquad i = 1, 2. \qquad [35]$$

Accounting for the initial and boundary conditions 9 with $c_{\text{in}} = 0$, the Laplace-transformed solutions of Eq. 35 are

$$\hat{u}_1(r, \lambda) = A_1(\mathrm{e}^{-\sqrt{\lambda/D_1}\, r} - \mathrm{e}^{\sqrt{\lambda/D_1}\, r}), \quad 0 \leqslant r \leqslant r_1, \qquad [36]$$

and

$$\hat{u}_2(r, \lambda) = A_2\, \mathrm{e}^{\sqrt{s}\, r} + B_2\, \mathrm{e}^{-\sqrt{s}\, r}, \quad r_1 \leqslant r \leqslant r_2, \qquad [37]$$

where λ is the Laplace variable, and $s = \lambda/D_2$. The constants of integration A_1, A_2, and B_2 are obtained from the Laplace transforms of the auxiliary conditions 3, 15, and 24,

$$D_2\frac{\mathrm{d}\hat{c}_2}{\mathrm{d}r}(r_2,\,\lambda)=\frac{J}{\lambda},$$
$$D_1\frac{\mathrm{d}\hat{c}_1}{\mathrm{d}r}(r_1,\,\lambda)=D_2\frac{\mathrm{d}\hat{c}_2}{\mathrm{d}r}(r_1,\,\lambda)$$
$$=\frac{r_2^2}{r_1^2}D_2\mathrm{e}^{-\lambda\tau}\frac{\mathrm{d}\hat{c}_2}{\mathrm{d}r}(r_2,\,\lambda). \qquad [38]$$

$$A_1=-\frac{Jr_2^2}{FD_1\lambda}\frac{\mathrm{e}^{-\lambda\tau}}{(r_1\sqrt{\lambda/D_1}\,+1)\mathrm{e}^{-\sqrt{\lambda/D_1}\,r_1}+(r_1\sqrt{\lambda/D_1}\,-1)\mathrm{e}^{\sqrt{\lambda/D_1}r_1}}; \qquad [39]$$

with $\beta=r_2-r_1$, and

$$A_2=\frac{Jr_2^2}{FD_2\lambda}$$
$$\times\frac{\mathrm{e}^{\beta\sqrt{s}}(r_1+1/\sqrt{s})-\mathrm{e}^{-D_2\tau s}(r_2+1/\sqrt{s})}{(r_2-1/\sqrt{s})\mathrm{e}^{\beta\sqrt{s}}(r_1\sqrt{s}\,+1)-(r_1-1/\sqrt{s})\mathrm{e}^{-\beta\sqrt{s}}(r_2\sqrt{s}\,+1)}\mathrm{e}^{-r_2\sqrt{s}} \qquad [40]$$

$$B_2=\frac{Jr_2^2}{FD_2\lambda}$$
$$\times\frac{\mathrm{e}^{-\beta\sqrt{s}}(r_1-1/\sqrt{s})-\mathrm{e}^{-D_2\tau s}(r_2-1/\sqrt{s})}{(r_2-1/\sqrt{s})\mathrm{e}^{\beta\sqrt{s}}(r_1\sqrt{s}\,+1)-(r_1-1/\sqrt{s})\mathrm{e}^{-\beta\sqrt{s}}(r_2\sqrt{s}\,+1)}\mathrm{e}^{r_2\sqrt{s}}. \qquad [41]$$

We rewrite Eqs. 36–41 as Eq. 25.

Solution for equivalent sphere.—Introducing the new dependent variable $u(r,\,t)=rc(r,\,t)$ and the rescaled time

$$T=\int_0^t D^*(t')\mathrm{d}t', \qquad [42]$$

we transform Eq. 10 into

$$\frac{\partial u}{\partial T}=\frac{\partial^2 u}{\partial r^2},\qquad 0<r<r_2. \qquad [43]$$

Accounting for the boundary and initial conditions 14 with $c_{\mathrm{in}}=0$, the Laplace-transformed (with respect to T) solution of this equation is

$$\hat{u}(r,\,\lambda_T)=A(\mathrm{e}^{-r\sqrt{\lambda_T}}-\mathrm{e}^{r\sqrt{\lambda_T}}). \qquad [44]$$

where λ_T is the Laplace-transform variable. The constant of integration A is obtained from the Laplace transform of the boundary condition 24,

$$\frac{\mathrm{d}(\hat{u}/r)}{\mathrm{d}r}(r_2,\,t)=\frac{J}{F}\int_0^\infty\frac{\mathrm{e}^{-\lambda_T T}}{D^*(h(T))}\,\mathrm{dT}. \qquad [45]$$

where $t=h(T)$ is given implicitly by Eq. 42. This step leads to

$$A=\frac{J}{F}\frac{r_2^2}{\mathrm{e}^{r_2\sqrt{\lambda_T}}-\mathrm{e}^{-r_2\sqrt{\lambda_T}}-r_2\sqrt{\lambda_T}(\mathrm{e}^{-r_2\sqrt{\lambda_T}}+\mathrm{e}^{r_2\sqrt{\lambda_T}})}$$
$$\times\int_0^\infty\frac{\mathrm{e}^{-\lambda_T T}}{D^*(h(T))}\,\mathrm{dT} \qquad [46]$$

and, ultimately, to Eq. 26.

Numerical algorithm for solving $D^*(t)$.—Rewrite Eq. (29) in terms of t:

$$\frac{Jr_2}{F}\int_0^t w(r_2,\int_{v't}D^*(t')\mathrm{d}t')\mathrm{d}v'$$
$$=V_1c_1(r_1,\,t)+(1-V_1)c_2(r_2,\,t) \qquad [47]$$

Algorithm 1. Numerical algorithm for computing $D^*(t)$

For $k=1$:
1. Take the inverse Laplace transform of Eq. 25 to obtain $c_1(r_1,\,t_1)$ and $c_2(r_2,\,t_1)$
2. Compute $c(r_2,\,t_1)$ in Eq. 28
3. Solve equation $c(r_2,\,t_1)=\frac{Jr_2}{F}w(r_2,\,\frac{\Delta t}{2}D^*(t_1))\Delta t$ for $D^*(t_1)$, where w is given by Eq. 27b

For $k=2$ to N_t:
1. Take the inverse Laplace transform of Eqs. 25 to obtain $c_1(r_1,\,t_k)$ and $c_2(r_2,\,t_k)$
2. Compute $c(r_2,\,t_k)$ in Eq. 28
3. Solve for $D^*(t_k)$ from equation:
$c(r_2,\,t_k)=\frac{Jr_2}{F}\sum_{j=1}^k w(r_2,\,\sum_{i=1}^j D^*(t_{k-i+1})\Delta t\cdot l)\Delta t$,
$l=\begin{cases}1/2, & \text{if } i=j\\ 1, & \text{if } i\neq j\end{cases}$
where w is given by Eq. 27b
3. Stop at the kth iteration if $t_k>\tau$ and $\left|\frac{D^*(t_k)-D^*(t_{k-1})}{D^*(t_{k-1})}\right|\leqslant 10^{-6}$ as D^* reaches steady state

Asymptotic expressions for large time.—For large t, i.e., for small λ, the interfacial Li-ion concentrations in the composite sphere, Eq. 25, behaves asymptotically as

$$\hat{c}_1(r_1,\,\lambda)=\frac{Jr_2^2}{r_1^3F}\left[\frac{3}{\lambda^2}-\frac{(15D_1\tau-r_1^2)}{5\lambda D_1}\right]+\mathcal{O}(\lambda^{3/2}), \qquad [48a]$$

$$\hat{c}_2(r_2,\,\lambda)=\frac{Jr_2}{2D_2F\lambda}\left[\frac{\beta^3+3\beta^2r_1+6D_2r_2\tau}{\beta^3+3\beta r_1r_2}+\mathcal{O}(\lambda^{1/2})\right] \qquad [48b]$$

$$\hat{c}_2(r_1,\,\lambda)=\frac{Jr_2^2}{2FD_2r_1\lambda}\left[\frac{\beta^3-3\beta^2r_1+6D_2r_1\tau}{\beta^3+3\beta r_1r_2}+\mathcal{O}(\lambda^{1/2})\right]. \qquad [48c]$$

Its inverse Laplace transform is

$$c_1(r_1,\,t)\approx\frac{Jr_2^2}{r_1^3F}\left[-\frac{(15D_1\tau-r_1^2)}{5D_1}+3t\right],$$
for large t; [49a]

$$c_2(r_2,\,t)\approx\frac{Jr_2}{2D_2F}\left\{\frac{\beta^3+3\beta^2r_1+6D_2r_2\tau}{\beta^3+3\beta r_1r_2}+\mathcal{O}(1/\sqrt{t})\right\},$$
for large t [49b]

$$c_2(r_1,\,t)\approx\frac{Jr_2^2}{2FD_2r_1}\left\{\frac{\beta^3-3\beta^2r_1+6D_2r_1\tau}{\beta^3+3\beta r_1r_2}+\mathcal{O}(1/\sqrt{t})\right\},$$
for large t. [49c]

Similarly, for the homogenized sphere with constant diffusion coefficient D^*, the large-time approximation of Eq. 27 is

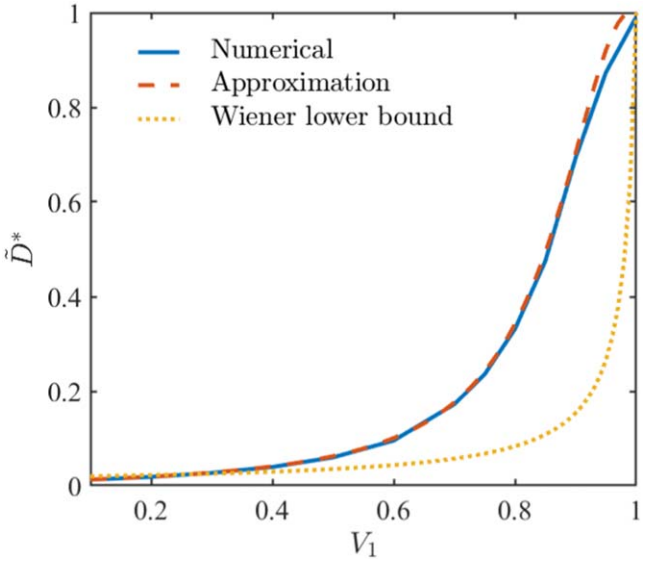

Figure 7. Steady-state effective diffusion coefficient $\tilde{D}^*$ alternatively computed as the numerical solution of Eq. 29, the analytical expression 31 and the Wiener lower bound 53. It is plotted as function of the active material's volume fraction V_1, for $D_2/D_1 = 0.0178$.

$$c(r_2, t) = \frac{3J}{r_2 F} t + \frac{J r_2}{5 D^* F}, \quad \text{for large } t. \tag{50}$$

Substitution of Eqs. 49 and 50 into Eq. 28 leads to

$$\frac{J r_2}{5 D^* F} = -\frac{(15 D_1 \tau - r_1^2) J}{5 D_1 r_2 F} + (1 - V_1) \frac{J r_2}{2 D_2 F} \frac{\beta^3 + 3\beta^2 r_1 + 6 D_2 r_2 \tau}{\beta^3 + 3 r_1 r_2 \beta}, \tag{51}$$

which yields

$$D^* = \left\{ \frac{r_1^2}{D_1 r_2^2} + \frac{5 V_2}{D_2} \left[\frac{(r_2 - r_1)^2 + 3(r_1 + 2r_2)(r_2 - r_1)}{2(r_2 - r_1)^2 + 6 r_1 r_2} - \frac{3(r_2 - r_1)^2}{V_2 r_2^2} \right] \right\}^{-1}. \tag{52}$$

Expressing this relation in terms of the volume fraction V_1 gives Eq. 31. Figure 7 shows that this analytical expression for $\tilde{D}^*$ is in close agreement with the numerical solution of Eq. 29 for the volume fraction V_1 ranging from 0.1 to 1.0. The close agreement between the two solutions serves to verify the accuracy of the numerical solution of Eq. 29. It also suggests the possibility of using the readily computable expression 31 as the value of the equivalent diffusivity of composite spheres in battery-scale models.

It is worthwhile to compare our analytical expression for $\tilde{D}^*$ in Eq. 31 with the Wiener lower bound,

$$D_W^* = (V_1/D_1 + V_2/D_2)^{-1}. \tag{53}$$

Both are weighted harmonic means of D_1 and D_2, but with different weights. The weights in the Wiener bound are the volume fractions of the two materials, while those in our expression are more evolved because they account for Li-ion intercalation. Figure 7 shows that our expression for the equivalent diffusivity given by Eq. 31 is considerably more accurate than its counterpart predicted by the Wiener bound in Eq. 53 for the full range of the active material's volume fraction V_1 (Fig. 7). The latter's error is highest when $0.8 < V_1 < 0.95$, which is a typical range for the volume fraction of active material in most electrodes. This result highlights the advantage of using Eq. 31 for battery modeling as a means to guarantee the mass and charge conservation in the presence of ion intercalation in active particles.

Substitution of Eqs. 49 into Eq. 30 gives

$$\frac{c^*_{\max}(t)}{c_{1,\max}} = V_1 \frac{15 D_1 (t - \tau) + r_1^2}{15 D_1 t + r_1^2} + V_2 \frac{5 r_1 (r_2 - r_1)}{2 r_2 (15 D_2 t / r_1^2 + D_2/D_1)} \times \frac{2 r_1 + 7 r_2}{(r_2 - r_1)^2 + 3 r_1 r_2} \tag{54}$$

and

$$\frac{k^*(t)}{k_1} = \frac{r_1^2}{r_2^2} \sqrt{\frac{r_2 + 2r_1}{7r_2 + 2r_1}} \sqrt{\frac{c_{1,\max}}{c^*_{\max}(t)}} \approx \frac{r_1^2}{r_2^2} \sqrt{\frac{r_2 + 2r_1}{7r_2 + 2r_1} V_1} = V_1^{2/3} \sqrt{\frac{1 + 2V_1^{1/3}}{7 + 2V_1^{1/3}} V_1}. \tag{55}$$

Since $t \gg \tau$ and $V_1 \gg V_2$, we obtain approximations 32 and 33.

ORCID

Daniel M. Tartakovsky https://orcid.org/0000-0001-9019-8935

References

1. G. Plett, *Battery Management Systems, Volume I: Battery Modeling* (Artech House, Boston, MA) (2015).
2. M. Indrikova, S. Grunwald, F. Golks, A. Netz, B. Westphal, and A. Kwade, "The Morphology of Battery Electrodes with the Focus of the Conductive Additives Paths." *J. Electrochem. Soc.*, **162**, A2021 (2015).
3. M. Wu et al., "Toward an ideal polymer binder design for high-capacity battery anodes." *J. Am. Chem. Soc.*, **135**, 12048 (2013).
4. J. Chen, J. Liu, Y. Qi, T. Sun, and X. Li, "Unveiling the roles of binder in the mechanical integrity of electrodes for lithium-ion batteries." *J. Electrochem. Soc.*, **160**, A1502 (2013).
5. G. Liu, H. Zheng, S. Kim, Y. Deng, A. M. Minor, X. Song, and V. S. Battaglia, "Effects of various conductive additive and polymeric binder contents on the performance of a lithium-ion composite cathode." *J. Electrochem. Soc.*, **155**, A887 (2008).
6. D. E. Stephenson, B. C. Walker, C. B. Skelton, E. P. Gorzkowski, D. J. Rowenhorst, and D. R. Wheeler, "Modeling 3D Microstructure and Ion Transport in Porous Li-Ion Battery Electrodes." *J. Electrochem. Soc.*, **158**, 781 (2011).
7. N. A. Zacharias, D. R. Nevers, C. Skelton, K. Knackstedt, D. E. Stephenson, and D. R. Wheeler, "Direct Measurements of Effective Ionic Transport in Porous Li-Ion Electrodes." *J. Electrochem. Soc.*, **160**, A306 (2013).
8. M. Kroll, S. L. Karstens, M. Cronau, A. Hölzel, S. Schlabach, N. Nobel, C. Redenbach, B. Roling, and U. Tallarek, "Three-Phase Reconstruction Reveals How the Microscopic Structure of the Carbon-Binder Domain Affects Ion Transport in Lithium-Ion Batteries." *Batteries & Supercaps*, **4**, 1363 (2021).
9. X. Lu et al., "3D microstructure design of lithium-ion battery electrodes assisted by X-ray nano-computed tomography and modelling." *Nat. Commun.*, **11**, 12 (2020).
10. B. L. Trembacki, A. N. Mistry, D. R. Noble, M. E. Ferraro, P. P. Mukherjee, and S. A. Roberts, "Editors' Choice–Mesoscale Analysis of Conductive Binder Domain Morphology in Lithium-Ion Battery Electrodes." *J. Electrochem. Soc.*, **165**, E725 (2018).
11. F. L. E. Usseglio-Viretta et al., "Resolving the discrepancy in tortuosity factor estimation for li-ion battery electrodes through micro-macro modeling and experiment." *J. Electrochem. Soc.*, **165**, A3403 (2018).
12. S. Hein et al., "Influence of Conductive Additives and Binder on the Impedance of Lithium-Ion Battery Electrodes: Effect of Morphology." *J. Electrochem. Soc.*, **167**, 013546 (2020).
13. G. Richardson, I. Korotkin, R. Ranom, M. Castle, and J. M. Foster, "Generalised single particle models for high-rate operation of graded lithium-ion electrodes: Systematic derivation and validation." *Electrochimica Acta*, **339**, 135862 (2020).
14. S. G. Marquis, V. Sulzer, R. Timms, C. P. Please, and S. J. Chapman, "An asymptotic derivation of a single particle model with electrolyte." *J. Electrochem. Soc.*, **166**, A3693 (2019).

15. M. Guo, G. Sikha, and R. E. White, "Single-particle model for a lithium-ion cell: Thermal behavior." *J. Electrochem. Soc.*, **158**, A122 (2010).
16. J. Li, N. Lotfi, R. G. Landers, and J. Park, "A single particle model for lithium-ion batteries with electrolyte and stress-enhanced diffusion physics." *J. Electrochem. Soc.*, **164**, A874 (2017).
17. M. Doyle, T. F. Fuller, and J. Newman, "Modeling of Galvanostatic Charge and Discharge of the Lithium/Polymer/Insertion Cell." *J. Electrochem. Soc.*, **140**, 1526 (1993).
18. W. Lai and F. Ciucci, "Mathematical modeling of porous battery electrodes-Revisit of Newman's model." *Electrochimica Acta*, **56**, 4369 (2011).
19. M. Schmuck, "Upscaling of Solid-electrolyte Composite Intercalation Cathodes for Energy Storage Systems." *Applied Mathematics Research eXpress*, **2017**, 402 (2017).
20. X. Zhang and D. M. Tartakovsky, "Effective ion diffusion in charged nanoporous materials." *J. Electrochem. Soc.*, **164**, E53 (2017).
21. Y. K. Lee, "The effect of active material, conductive additives, and binder in a cathode composite electrode on battery performance." *Energies*, **12**, 658 (2019).
22. G. W. Milton, *The Theory of Composites. Cambridge Monographs on Applied and Computational Mathematics* (Cambridge University Press, Cambridge) (2002).
23. T. R. Ferguson and M. Z. Bazant, "Nonequilibrium Thermodynamics of Porous Electrodes." *J. Electrochem. Soc.*, **159**, A1967 (2012).
24. Y. Hyun, S. P. Neuman, V. V. Vesselinov, W. A. Illman, D. M. Tartakovsky, and V. Di Federico, "Theoretical interpretation of a pronounced permeability scale effect in unsaturated fractured tuff." *Water Resour. Res.*, **38**, 28 (2002).
25. G. Severino and A. Coppola, "A note on the apparent conductivity of stratified porous media in unsaturated steady flow above a water table." *Transport in Porous Media*, **91**, 733 (2012).
26. S. Tozza and G. Toraldo, "Numerical hints for insulation problems." *Applied Mathematics Letters*, **123**, 107609 (2022).
27. U. Hornung, *Homogenization and porous media* (Springer, Berlin) 6 (2012).
28. K. Yamamoto, Y. Iriyama, T. Asaka, T. Hirayama, H. Fujita, C. A. J. Fisher, K. Nonaka, Y. Sugita, and Z. Ogumi, "Dynamic Visualization of the Electric Potential in an All-Solid-State Rechargeable Lithium Battery." *Angew. Chem. Int. Ed.*, **49**, 4414 (2010).
29. G. B. Less, J. H. Seo, S. Han, A. M. Sastry, J. Zausch, A. Latz, S. Schmidt, C. Wieser, D. Kehrwald, and S. Fell, "Micro-Scale Modeling of Li-Ion Batteries: Parameterization and Validation." *J. Electrochem. Soc.*, **159**, A697 (2012).
30. Juraj. Numerical inversion of laplace transforms in Matlab, 2022, https://www.mathworks.com/matlabcentral/fileexchange/32824-numerical-inversion-of-laplace-transforms-in-matlab.
31. D. M. Tartakovsky and S. P. Neuman, "Transient effective hydraulic conductivities under slowly and rapidly varying mean gradients in bounded three-dimensional random media." *Water Resources Research*, **34**, 21 (1998).
32. L. S. Kremer, A. Hoffmann, T. Danner, S. Hein, B. Prifling, D. Westhoff, C. Dreer, A. Latz, V. Schmidt, and M. Wohlfahrt-Mehrens, "Manufacturing Process for Improved Ultra-Thick Cathodes in High-Energy Lithium-Ion Batteries." *Energy Technology*, **8**, 1900167 (2020).